AGU100 ADVANCING EARTH AND SPACE SCIENCE

JGR Space Physics

RESEARCH ARTICLE

10.1029/2018JA026043

Key Points:

- Self-consistent magnetic field is obtained under a Gaussian distribution of thermal pressure
- The dependence of the magnetic dip depth on thermal pressure distribution is shown
- The change in the magnetic field topology by thermal pressure can lead to additional gradient drift

Correspondence to:
Z. Xia and L. Chen,
Zhiyang.Xia@utdallas.edu;
lunjin.chen@gmail.com

Citation:
Xia, Z., Chen, L., Artemyev, A. V., Zhu, H., Jordanova, V. K., & Zheng, L. (2019). The effects of localized thermal pressure on equilibrium magnetic fields and particle drifts in the inner magnetosphere. *Journal of Geophysical Research: Space Physics*, *124*. https://doi.org/10.1029/2018JA026043

Received 31 AUG 2018
Accepted 17 MAY 2019
Accepted article online 31 MAY 2019

The Effects of Localized Thermal Pressure on Equilibrium Magnetic Fields and Particle Drifts in The Inner Magnetosphere

Zhiyang Xia[1], Lunjin Chen[1], Anton Artemyev[2,3], Hui Zhu[1], Vania K. Jordanova[4], and Liheng Zheng[1]

[1]Department of Physics, University of Texas at Dallas, Richardson, TX, USA, [2]Institute of Geophysics and Planetary Physics, University of California, Los Angeles, CA, USA, [3]Space Research Institute, RAS, Moscow, Russia, [4]Los Alamos National Laboratory, Los Alamos, NM, USA

Abstract Localized injections of hot anisotropic plasma sheet particles into the inner magnetosphere can significantly deform the quiet time dipole-like magnetic field and thus disturb electron and ion's drift paths and scattering rates. Although many details of magnetic field deformation can be inferred from empirical models, roles of different characteristics of injected plasma on the structure of such deformation require further investigation. In this study, we use the 2-D axisymmetric equilibrium model to calculate self-consistent magnetic field in force balance with a Gaussian thermal pressure distribution characterized by four input parameters: the ratio between plasma pressure and magnetic pressure (β) at the pressure peak β_0, the radial location of the pressure peak L_0, the width of the half peak pressure σ_0, and the equatorial pressure anisotropy A_e. Using the modeled magnetic field, we find that the magnetic field perturbation increases with increasing β_0 and decreasing σ_0 while the magnetic curvature perturbation increases with increasing A_e, β_0, and σ_0 and decreasing L_0. For energetic particles the change of magnetic gradient drift motion is much greater than that of curvature drift motion. The magnetic dip structure formation requires a critical β value that increases with increasing σ_0 and decreasing L_0. Despite the unavailability of observations in the existing literatures to check the condition of magnetic dip formation, such condition will be checked against observations as a future study. Finally, we also use 3-D ring current-atmosphere interactions model with self-consistent magnetic field model to illustrate the effect of azimuthal pressure distribution, which is relevant to asymmetric ring current.

1. Introduction

The partial ring current generated by the asymmetric azimuthal drift of energetic ions and electrons exhibits diamagnetic effect on the Earth's magnetic field due to the force balance between thermal pressure of the hot particles and the background magnetic pressure, especially in the magnetic storm time (Fukushima & Kamide, 1973) when the ring current intensity increases and the plasma β value can reach about ~O(1). Ukhorskiy et al. (2006) has reported the magnetic dip structure, which is caused by the diamagnetic effect of the storm time partial ring current, as a local magnetic minimum followed by a magnetic island (local maximum) at larger L shell region from the TS05 model (Tsyganenko & Sitnov, 2005). This magnetic dip structure locates from midnight to post noon region in a few magnetic local time (MLT) hours and near 5–6 R_E with a width of ~2 R_E in the radial direction. The depth of the dip (absolute value of difference between the local minimum magnetic field and the quite time magnetic field) can reach about 50 nT.

The magnetic dip structure has been recently observed by the inner magnetosphere spacecraft. Xiong et al. (2017) provided a single satellite observation of magnetic dip generated by the injection of energetic ions during substorm by Van Allen Probes, with increased thermal pressure and decreased magnetic field. A butterfly pitch angle distribution of energetic electrons was found and explained as the result of inward transport of the relativistic electrons, which was caused by the magnetic gradient drift due to the magnetic dip. He et al. (2017) reported another magnetic dip event during the substorm using multiple-satellite observations. In this event, the magnetic dip together with the energetic ions moves at a speed comparable to the ion's drift velocity, which indicates that the magnetic dip structure is induced by the ring current ions. Excitation of electromagnetic ion cyclotron (EMIC) waves were also observed accompany with magnetic dip structures (He et al., 2017; Remya et al., 2018). According to linear theory analysis, the magnetic dip accompanied with high ion β and ion temperature anisotropy can provide a favorable condition for EMIC wave generation. Moreover, the center region of magnetic dip is a kind of “minimum-B-pockets” in the equatorial plane, which can generate whistler mode waves (Santolík, 2008; Tsurutani et al., 2009; Tenerani et al., 2013). Zhima et al. (2015) also observed whistler mode wave generating at the edges of magnetic dip, where positive temperature anisotropy and pancake distribution existed to provide free energy for growth of the whistler mode waves.

The magnetic field topology in the inner magnetosphere affects the drift motion of the energetic particles significantly because of dominant magnetic gradient and curvature drifts. The magnetic dip structure, comparing with empirical or analytic dipole magnetic fields, exhibits two significantly different features. The first one is the presence of an azimuthal magnetic field gradient, which causes radial drift. When eastward drifting energetic electrons encounters the magnetic dip structure, the azimuthal gradient of the magnetic dip causes the electrons to drift inward and results in the butterfly distribution as discussed in Xiong et al. (2017). Another difference is the radial gradient of magnetic field becomes positive (always negative for dipole field) at the radial outer edge of the magnetic dip. This inverse gradient may cause the inverse gradient drift motion. Although ring current protons and radiation belt electrons do not interact directly, the magnetic dip driven by the ring current provides an indirect way to affect the variability of radiation belt electron populations. Learning about the formation condition of magnetic dip structure and its influence to the energetic particles' drift motion can enhance our understanding of dynamic processes in the inner magnetosphere.

Equilibrium magnetosphere models are widely used to calculated three-dimensional (3-D) self-consistent magnetic field (SCB) that holds force balance with plasma pressure in the inner magnetosphere (Jordanova et al., 2010; Yu et al., 2012; Zaharia et al., 2006) and in the plasma sheet (Yue et al., 2013, 2014, 2015). Both spacecraft observations and inner magnetosphere models indicate that, as L shell increases, the thermal pressure of ring current increases to a peak value and then decreases (Chen et al., 2010; De Michelis et al., 1999; Godinez et al., 2016; Imajo et al., 2018). Thus, we can use a Gaussian distribution to approximate the radial pressure distribution. Our previous work (Xia et al., 2017) used a 2-D axisymmetric equilibrium model to calculate SCB under a radial Gaussian thermal pressure and investigated instability condition for field line resonance, which favored more negative radial gradient of plasma pressure. It also showed that sufficiently large plasma β (ratio between plasma pressure and magnetic pressure) could result in the change of magnetic field topology and even formation of the local magnetic minimum (magnetic dip). In this study, we systematically study the effects of the Gaussian thermal pressure distribution on the magnetic field configuration (and magnetic dip formation) and the resulting changes in particle magnetic gradient and curvature drifts. There are four parameters determining the pressure distribution: the location of the pressure peak L_0, the β value at the pressure peak β_0, the width of half pressure peak σ_0, and the equatorial pressure anisotropy A_e. In addition, we also use the 3-D ring current-atmosphere interactions model with SCB (RAM-SCB) model (Jordanova et al., 2010) to study the influence of the azimuthal pressure distribution, which is characterized by the four parameters above and another parameter, the MLT width of half pressure peak in the azimuthal direction σ_{MLT}. The purpose of this study is to construct a comprehensive understanding of the relationship between the configuration of Earth's magnetic field and the ring current plasma pressure, and to estimate the relative perturbation of magnetic drift motions under this pressure and the critical condition to form the magnetic dip structure.

2. Axisymmetric Equilibrium Model

2.1. Equilibrium Magnetic Field Model Description

The axisymmetric equilibrium model used in this study is the same as that in our previous work (Xia et al., 2017), whose basic theory had been discussed in the work of Cheng (1992) and Zaharia et al. (2004). The basic magnetohydrodynamics equations to be solved for the pressure equilibrium are

$$\mathbf{J} \times \mathbf{B} = \nabla \cdot \mathbf{P} \tag{1}$$

$$\nabla \times \mathbf{B} = \mu_0 \mathbf{J} \tag{2}$$

$$\nabla \cdot \mathbf{B} = 0, \tag{3}$$

where $\mathbf{J}$ is the current, $\mathbf{B}$ is the magnetic field, μ_0 is the vacuum permeability, and $\mathbf{P}$ is the anisotropic thermal pressure tensor that can be represented as $P_\perp \mathbf{I} - (P_\perp - P_\parallel)\hat{b}\hat{b}$, where $\mathbf{I}$ is the unit tensor, $\hat{b} = \mathbf{B}/B$ is the unit vector of the magnetic field, and $P_\perp$ and $P_\parallel$ are the perpendicular and parallel pressure components. The magnetic field $\mathbf{B}$ is divergence-free according to equation (3) and can be expressed in terms of two Euler potential ψ and α as $\mathbf{B} = \nabla\psi \times \nabla\alpha$. Thus, $\mathbf{B}$ is perpendicular to both $\nabla\psi$ and $\nabla\alpha$ and the intersections of constant ψ and constant α surfaces correspond to magnetic field lines. In our model, we choose the magnetic flux as ψ and the azimuthal angle as α for the axisymmetric fields.

The computation coordinates are curvilinear flux coordinates corresponding to ψ (radial direction), α (azimuthal direction), and the length along field line (field line direction), which had been introduced in Xia et al. (2017). Eventually, equation (1) can be reduced to the form to be solved for ψ in the meridian $(X - Z)$ plane:

$$\mu_0 \mathbf{J} \cdot \nabla\alpha = \nabla \cdot [(\nabla\alpha \cdot \nabla\psi)\nabla\alpha - (\nabla\alpha)^2 \nabla\psi] = -\frac{\mathbf{B} \times \nabla\alpha}{\sigma_P B^2} \cdot \left[\mu_0 \nabla P_\perp + (1 - \sigma_P)\nabla\left(\frac{B^2}{2}\right)\right], \tag{4}$$

where $\sigma_P = 1 + \mu_0(P_\perp - P_\parallel)/B^2$.

The pressure along the field line at an arbitrary location, including the perpendicular component $P_\perp$ and parallel component $P_\parallel$, can be obtained from the equatorial value of the anisotropic pressure through the assumption of Maxwellian plasma distribution (Tsyganenko, 2000; Xiao & Feng, 2006):

$$P_\perp = \frac{P_{\perp e}}{[1 + A_e(1 - S)]^2} \tag{5}$$

$$P_\parallel = \frac{P_{\parallel e}}{1 + A_e(1 - S)} \tag{6}$$

$$A = \frac{1}{1 + A_e(1 - S)} - 1, \tag{7}$$

where $S = B_e/B$ is the ratio between the magnitudes of the equatorial magnetic field B_e and the magnetic field at the location of interest B, $A = P_\perp/P_\parallel - 1$ is the anisotropy, the subscript “e” denotes the value in the equatorial plane. A Gaussian distribution $P_e(x) = P_0 \exp[-(x - L_0)^2/2\sigma_0^2]$ is used to approximate the thermal pressure of the symmetric ring current, where $P_e = (2P_{\perp e} + P_{\parallel e})/3$ is the average pressure in the equatorial plane, P_0, L_0, and σ_0 are the peak pressure, the location of the pressure peak, and the width of the half pressure peak respectively. The value of P_0 is set to be $\beta_0 P_{\text{mag}}$, where P_{mag} is the magnetic pressure at L_0, and β_0 is the constant β at L_0. Thus, the equatorial distribution of plasma pressure in our model can be determined by these four parameters: L_0, σ_0, β_0, and A_e. The case of $\beta_0 = 0$ represents the cold plasma case (the dipole field) and the $A_e = 0$ case represents the isotropic pressure case.

After iteratively solving equation (4) for the distribution of ψ and the corresponding $\mathbf{B}$ in the meridian plane, we can finally reach a equilibrium state, which satisfies the convergence condition $\Delta = \Sigma_{i,j}|[\psi_{i,j}(n) - \psi_{i,j}(n-1)]/\psi_{i,j}(n-1)| < 2\times10^{-5}$, where i and j are the grid indices for the radial and field line directions respectively, n is the iteration number of the calculation, and Δ measures the relative difference between the current step n and the previous step $(n - 1)$. The domain of our equilibrium model is set to be $[3R_E, 9R_E]$, which is large enough to make sure the plasma pressures at the boundaries are nearly zero. The numbers of grids are 151 in the radial direction and 181 in the field line direction to ensure sufficient accuracy. The magnetic field for the initial step of the iterative method and the boundary magnetic field at the inner, outer, north, and south boundaries are set to be the Earth's dipole field. As the magnetic field is updated at each iteration step, the value of P_0 is also adjusted so that the value of β_0 can keep constant.

2.2. Example of the SCB Model

Figure 1 shows an example of model result for the case with $\beta_0 = 0.8$, $\sigma_0 = 0.4R_E$, $L_0 = 5$, and $A_e = 0$. Figure 1a shows the average pressure distribution in the meridional plane, and Figure 1b shows the corresponding topology of equilibrium magnetic field lines (the red solid lines), with the dipole field lines (the black dashed lines) also shown as a comparison. As the force equilibrium develops, the magnetic field lines expand from the peak pressure location $(L_0 = 5)$ inward and outward due to the thermal pressure, leading to weakened magnetic field strength there. In Figure 1c, the variations of β (the black line) and of the normal-

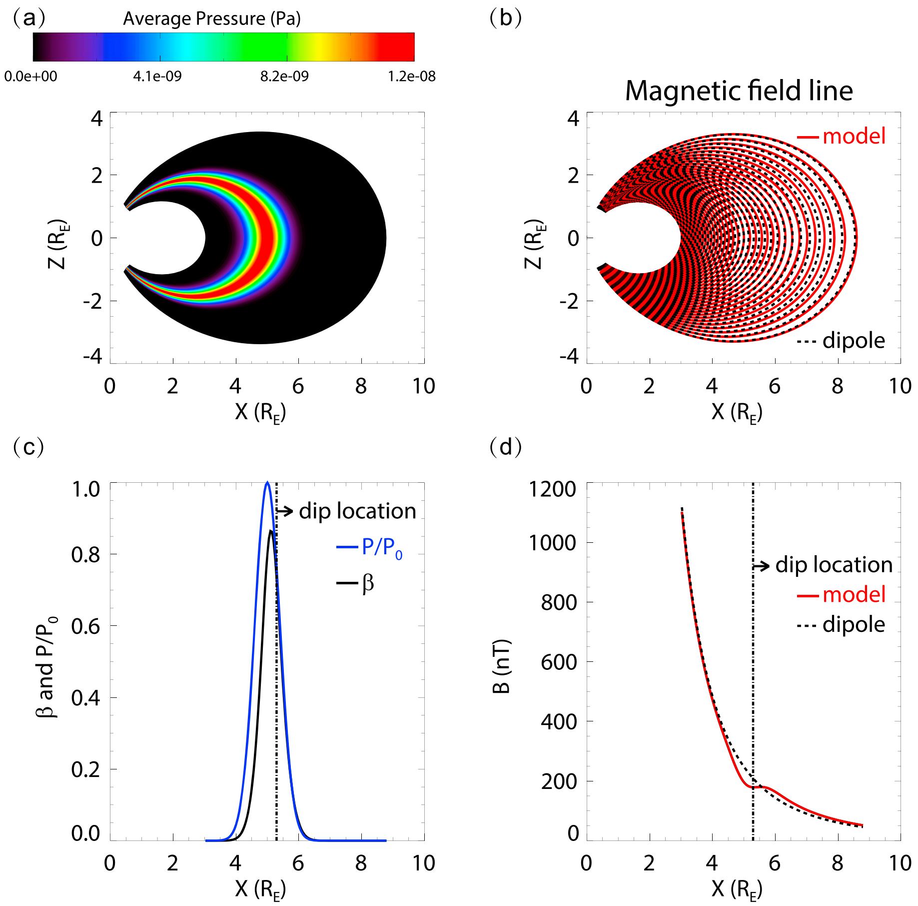

Figure 1. Model result for case with $\beta_0 = 0.8$, $\sigma_0 = 0.4\,R_E$, $L_0 = 5$ and $A_e = 0$. (a) The pressure distribution in the meridional plane. (b) The topologies of the modeled magnetic field lines (red solid lines) and dipole field lines (black dashed lines). (c) The variation of β versus x in the equator (black line) and the variation of normalized pressure versus x (blue line). (d) The variation of modeled magnetic field strength versus x in the equator (red solid line) and the variation of dipole field strength versus x (black dashed line).

ized pressure (the blue line, normalized by the pressure peak) at the equator are shown as functions of x. The peak of β is slightly outside the peak of the normalized pressure at L_0, because the magnetic field strength decreases as x increases. In Figure 1d, the variations of modeled (the red solid line) and dipole (the black dashed line) magnetic field strength at the equator are compared. Unlike monotonically decreasing dipole magnetic field, the modeled magnetic field exhibits a local minimum at about $x = 5.3R_E$ (labeled by the vertical dash-dotted lines in Figures 1c and 1d), outward of the peaks of plasma pressure and β (Figure 1c). The absolute value of difference between the modeled and dipole magnetic field strength $|\Delta B|$ at the local minimum is about 50 nT, comparable to the Tsyganeko empirical model results noted by Ukhorskiy et al. (2006).

3. Results of the SCB Model

3.1. Parametric Dependence of Magnetic Configuration

Here we study the effects of β_0, L_0, σ_0, and A_e on the magnetic field configuration, by changing one of the four parameters at a time while keeping the rest three fixed as the nominal case shown in Figure 2. Figures 2a and 2b show the variations of modeled equatorial magnetic field strength (B) versus x for cases with varying $\sigma_0 = 0.2, 0.3, 0.4, 0.5, 0.6\,R_E$ (Figure 2a) and for cases with varying $L_0 = 4.0, 4.5, 5.0, 5.5, 6.0$ (Figure 2b). Figures 2c and 2d show the corresponding normalized differences between modeled and dipole magnetic fields ($\Delta B/B_{\text{dipole}}$, where $\Delta B = B - B_{\text{dipole}}$ and the subscript *dipole* represents the dipole field). One can see that magnetic dip structure occurs for small values of σ_0 (0.2–0.4 R_E) from Figure 2a, and for almost all cases with different L_0 values from Figure 2b. The detailed effects of σ_0 and L_0 on the magnetic dip formation

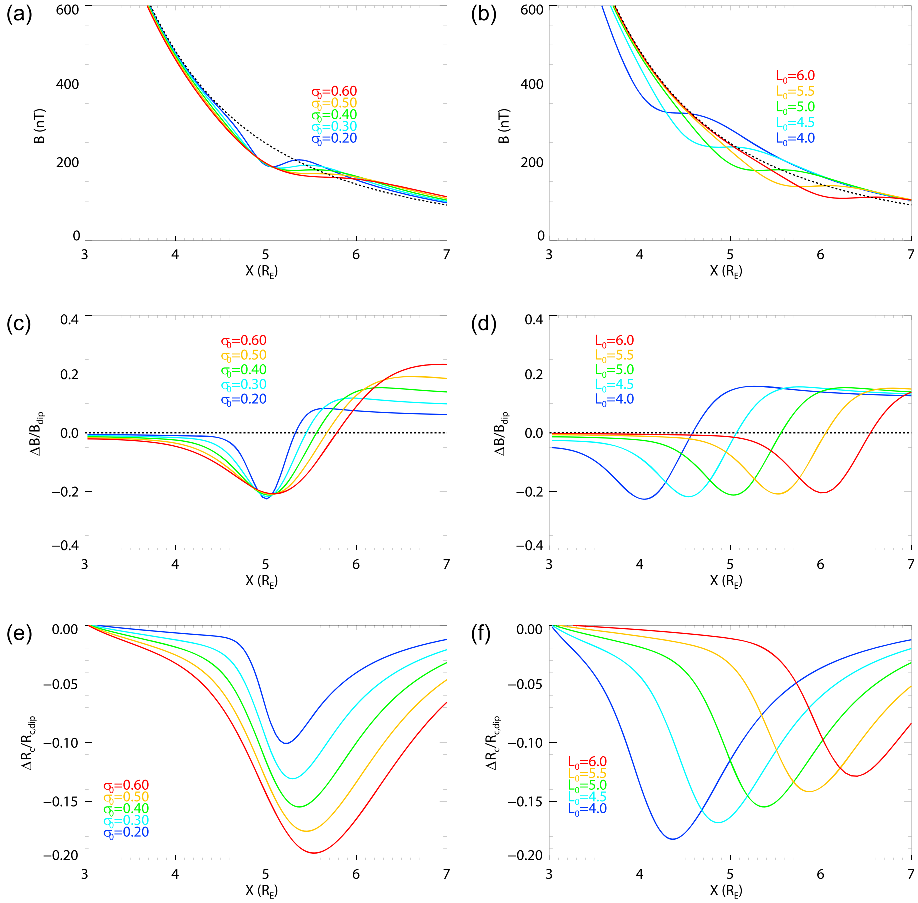

Figure 2. The variations of modeled magnetic field strength versus x in the equator for cases with (a) $\beta_0 = 0.8$, $A_e = 0,\ L_0 = 5, \sigma_0 = 0.2, 0.3, 0.4, 0.5, 0.6\ R_E$ and (b) $\beta_0 = 0.8,\ A_e = 0, \sigma_0 = 0.2\ R_E,\ L_0 = 4.0, 4.5, 5.0, 5.5, 6.0$. (c and d) The variations of the normalized difference between modeled and dipole magnetic fields $\Delta B/B_{\mathrm{dipole}}$ versus x for the same cases in (a) and (b), respectively. (e and f) The variations of the normalized difference between the radius of curvature of modeled and dipole magnetic field $\Delta R_c/R_{c,\mathrm{dip}}$ versus x for the same cases in (a) and (b) respectively.

will be discussed in section 3.3 later. Figure 2c shows that for the same L_0, a smaller value of σ_0 leads to a narrower magnetic dip but with similar perturbation of $\Delta B/B_{\mathrm{dipole}}$ at the dip location. The effect of L_0 on $\Delta B/B_{\mathrm{dipole}}$ is less significant (Figure 2d), and the minimum value of $\Delta B/B_{\mathrm{dipole}}$ remains nearly constant except different dip locations. The dominant factor determining the minimum value of $\Delta B/B_{\mathrm{dipole}}$ should be β as noted in Xia et al. (2017).

Besides the magnetic field strength, the curvature of magnetic field line is also changed due to the presence of thermal pressure. We plot normalized difference of the radius of curvature $\Delta R_c/R_{c,\mathrm{dip}} = (R_c - R_{c,\mathrm{dip}})/R_{c,\mathrm{dip}}$, in Figures 2e and 2f. The value of $R_{c,\mathrm{dip}}$ equals to $L/3$ for dipole field, where L is the L shell value. The value of R_c can be calculated from the model results by $R_c = 1/|\mathbf{b} \cdot \nabla \mathbf{b}|$, where $\mathbf{b} = \mathbf{B}/B$ is the magnetic field unit vector. The results show that R_c decreases by up to about 20% at the region outside L_0, and a larger value of σ_0 and a smaller value of L_0 favor enlarging the perturbation of the curvature.

After learning the dependence on σ_0 and L_0, we now focus on the role of the equatorial anisotropy A_e. The variations of B, $\Delta B/B_{\mathrm{dipole}}$, and $\Delta R_c/R_{c,\mathrm{dip}}$ for varying $A_e = -0.4, 0.0, 1.0, 2.0, 3.0, 4.0$ are shown in Figures 3a–3c, respectively. As A_e increases, the normalized magnetic perturbation ($\Delta B/B_{\mathrm{dipole}}$) varies only slightly. This can be explained by that the magnetic perturbation is mainly controlled by the gradient of the perpendicular thermal pressure ($P_\perp$) instead of the anisotropy (Xia et al., 2017). The effect of A_e on the field line curvature, however, is much more significant. For a large value of $A_e = 4.0$, $\Delta R_c/R_{c,\mathrm{dip}}$ can even change its sign and reach a positive value up to about 0.3 inside the pressure peak. Outside the pressure peak, the relative change in curvature radius becomes more negative as A_e increases.

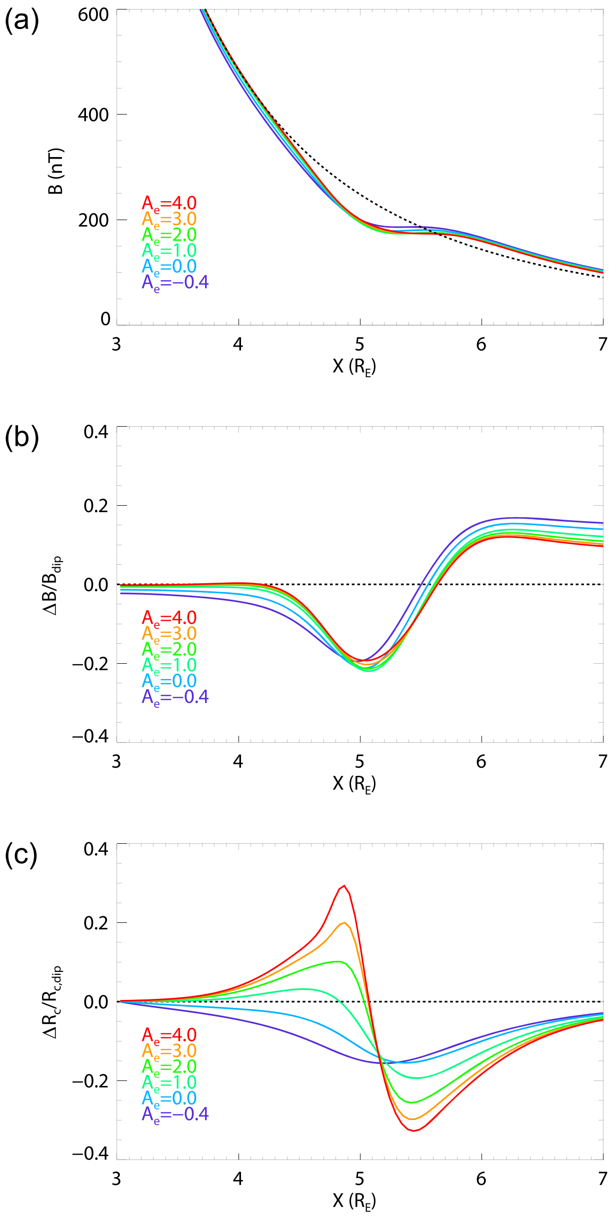

Figure 3. The variations of (a) B, (b) $\Delta B/B_{\text{dipole}}$, and (c) $\Delta R_c/R_{c,\text{dip}}$ versus x for cases with $L_0 = 5$, $\beta_0 = 0.8$, $\sigma_0 = 0.4R_E$, and $A_e = -0.4, 0.0, 1.0, 2.0, 3.0, 4.0$.

For the effect of β on the change of magnetic field strength and magnetic field line curvature, we make model runs for 3,000 combinations of four parameters, 5 values of L_0 ranging from 4 to 6, 24 values of β_0 ranging from 0.01 to 1.0, 5 values of σ_0 ranging from 0.2 to 0.6 R_{E}, and 5 values of A_e ranging from -0.4 to 0.4. For each run, we make scatter plots of minimum $\Delta B/B_{\text{dipole}}$ versus peak β value β_{peak} and minimum $\Delta R_c/R_{c,\text{dip}}$ versus β_{peak}, shown by Figures 4a and 4b, respectively. The figures show that the magnitudes of both minimum $\Delta B/B_{\text{dipole}}$ and minimum $\Delta R_c/R_{c,\text{dip}}$ increase as β_{peak} increases. For $\Delta B/B_{\text{dipole}}$, we make a polynomial fit for all the points, which is $(\Delta B/B_{\text{dipole}})_{\min} = -0.339\beta_{\text{peak}} + 0.112\beta^2_{\text{peak}}$ and plotted as the solid line in Figure 4a. For $\Delta R_c/R_{c,\text{dip}}$, we also obtained a linear fitted line with slope of about -0.214 and plot it as the solid line in Figure 4b.

3.2. The Effects of Magnetic Perturbation on Gradient and Curvature Drifts

At the presence of spatially varying magnetic field, charged particles experience magnetic gradient and curvature drift across field lines, due to the gradient of magnetic field strength and the curvature of magnetic field line, respectively. The drift velocities of gradient and curvature drifts for a relativistic particle can be

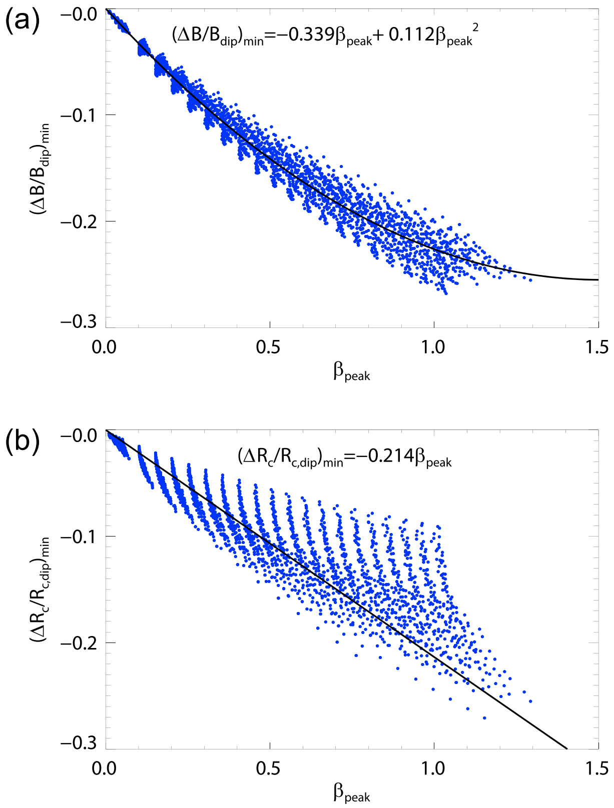

Figure 4. Scatter plots of (a) minimum $\Delta B/B_{\mathrm{dip}}$ versus β_{peak} and (b) minimum $\Delta R_c/R_{c0}$ versus β_{peak}. The dots in the figure represent all the cases with L_0 from 4 to 6, β_0 from 0.01 to 1.0, σ_0 from 0.2 to 0.6 R_E, and A_e from −0.4 to 0.4.

expressed, respectively, as

$$\mathbf{v}_g = \frac{\gamma m v_\perp^2}{2qB} \frac{\mathbf{B} \times \nabla B}{B^2} \tag{8}$$

and

$$\mathbf{v}_c = \frac{\gamma m v_\parallel^2}{qB} \frac{\mathbf{R}_c \times \mathbf{B}}{R_c^2 B}, \tag{9}$$

where $\gamma = (1 - v^2/c^2)^{-(1/2)}$ is the relativistic factor, v is the particle speed, and $v_\perp$ and $v_\parallel$ are the speed components perpendicular and parallel to the background magnetic field. The direction of R_c is opposite to the direction of $\mathbf{b} \cdot \nabla \mathbf{b}$. The ring current thermal pressure leads to the change of the magnetic field configuration and thus introduces additional gradient and curvature drift motions. From equations (8) and (9), for the gradient drift and curvature drift velocities, particle-independent terms that are related to only the magnetic field configuration are $D_g = \mathbf{B} \times \nabla B/B^3$ and $D_c = \mathbf{R}_c \times \mathbf{B}/(R_c^2 B^2)$, respectively. The relative changes of the two terms at the equator to those for the dipole field are shown by Figures 5a and 5b respectively, for cases with $\beta_0 = 0.8$, $A_e = 0$, $L_0 = 5$, and varying $\sigma_0 = 0.2, 0.3, 0.4, 0.5, 0.6\ R_E$. The largest $\Delta D_c/D_{c,\mathrm{dip}}$ can be up to 0.5 for $\sigma_0 = 0.2\ R_{\mathrm{E}}$ case, while the variation of the gradient drift term is more significant. For the $\sigma_0 = 0.2\ R_{\mathrm{E}}$ case as an example, the relative change of the gradient drift term varies from ∼ 2 inside the pressure peak to ∼ −2 outside the pressure peak. The value less than −1 means the drift direction reverses.

We also evaluate the bounce-averaged magnetic gradient and curvature drift velocity, which depend on particle's equatorial pitch angle. Figure 5c shows the relative change of the bounce-averaged drift velocity to the dipole case $\Delta D_b/D_{b,\mathrm{dip}} = (D_b - D_{b,\mathrm{dip}})/D_{b,\mathrm{dip}}$, where D_b is the sum of the bounce-averaged gradient and curvature drift velocities. The equatorial pitch angle θ_E is set to be 45°. One can see that the change of bounce-averaged total drift velocity is also significant, up to ∼1 inside the peak and ∼ −1 outside the peak. The change of the bounce-averaged drift is less than the change of the gradient drift term shown in Figure 5a,

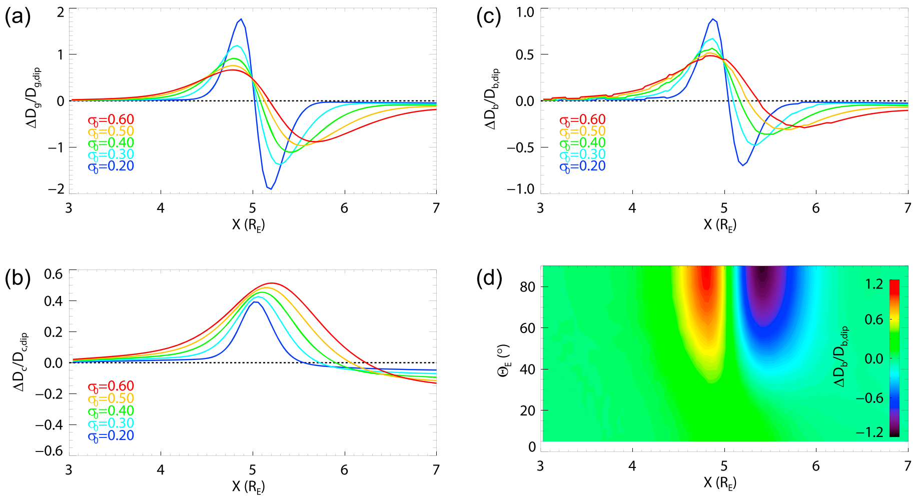

Figure 5. (a) The variations of normalized difference of D_g ($(D_g - D_{g,\mathrm{dip}})/D_{g,\mathrm{dip}}$) versus x for cases with $\beta_0 = 0.8,\ A_e = 0,\ L_0 = 5$, and $\sigma_0 = 0.2, 0.3, 0.4, 0.5, 0.6\ R_E$; (b) the variations of normalized difference of D_c versus x for the same cases. (c) The variations of normalized difference of bounce-averaged total drift velocity $\Delta D_b/D_{b,\mathrm{dip}} = (D_b - D_{b,\mathrm{dip}})/D_{b,\mathrm{dip}}$ versus x for the same cases. (d) The variations of bounce-averaged total drift velocity $\Delta D_b/D_{b,\mathrm{dip}}$ versus x and equatorial pitch angle θ_E for case with $\beta_0 = 0.8,\ \sigma_0 = 0.4\ R_E,\ A_e = 0,\ L_0 = 5$.

because the magnetic perturbation induced by the plasma pressure occurs predominately near the equator. Moreover, we also calculate the relative change of the bounce-averaged drift velocity for equatorial pitch angles from 5° to 90° by using the self-consistent magnetic field with $\sigma_0 = 0.4\ R_\mathrm{E},\ \beta_0 = 0.8,\ A_e = 0$ and $L_0 = 5$, which are shown by Figure 5d. The result shows that the change of the bounce-averaged drift is more significant for higher equatorial pitch angles because of dominant gradient drift over curvature drift and dominant magnetic perturbation near the equator over higher latitudes.

3.3. The Critical Condition for Magnetic Dip Formation

To examine the magnetic dip formation, we analyze the relationship between the normalized dip depth ($|\Delta B/B_\mathrm{dipole}|$ at the dip), if magnetic dip exists, and β_0 for cases with different L_0 and σ_0 values. The modeled results are shown in colored solid lines with dot symbols of Figure 6 for $\sigma_0 = 0.2, 0.4, 0.6\ R_\mathrm{E}$, respectively. One can see that when β_0 is small, there is no magnetic dip, represented by zero values of the normalized dip depth. When β_0 increases to a critical value, the dip structure may form. For cases with same σ_0, the critical value of β_0 decreases and the normalized dip depth increases as L_0 increases. Comparing among the three panels of Figure 6, for the same L_0 values, a smaller σ_0 results in a smaller critical β_0, and a larger normalized dip depth. When β_0 is sufficiently large, the normalized dip depth becomes independent of L_0.

The dependence of the critical β_0 on σ_0 and L_0 to form magnetic dips is also shown in Figure 7. As σ_0 increases or L_0 decreases, the critical β_0 tends to increase. The effect of σ_0 on the critical β_0 can be explained by comparing gradients of the background dipole field B_dipole and the perturbation magnetic field ΔB. If the gradient of ΔB (positive) balances that of B_dipole (negative), then the gradient of total magnetic field becomes 0, meaning the formation of magnetic dip. For the same L_0, a smaller σ_0 results in a larger gradient of ΔB (Figure 2c), which requires a smaller value of the critical β_0. The effect of L_0 on the critical β_0 can be understood as follows. Because $\Delta B/B_\mathrm{dipole}$ is independent of L_0 (Figure 2d), and the gradient of B_dipole is larger for smaller L_0, zero gradient of the total magnetic field requires a larger value of critical β_0 for smaller L_0. In summary, the model results indicate that the formation of magnetic dip needs a considerable pressure gradient, which is controlled by both the pressure peak value (corresponding to β_0) and the spatial scale of the pressure distribution (corresponding to σ_0). For smaller L shell region (closer to the Earth), since the gradient of background dipole field is larger, a larger thermal pressure gradient (corresponding to larger β_0 and smaller σ_0) is needed to produce magnetic field reduction that is large enough to form the magnetic dip.

Because simultaneous changes in magnetic field strength and magnetic field line curvature occur on top of dipolar fields, the solution to equation (4) of equilibrium magnetic field can only be obtained numerically.

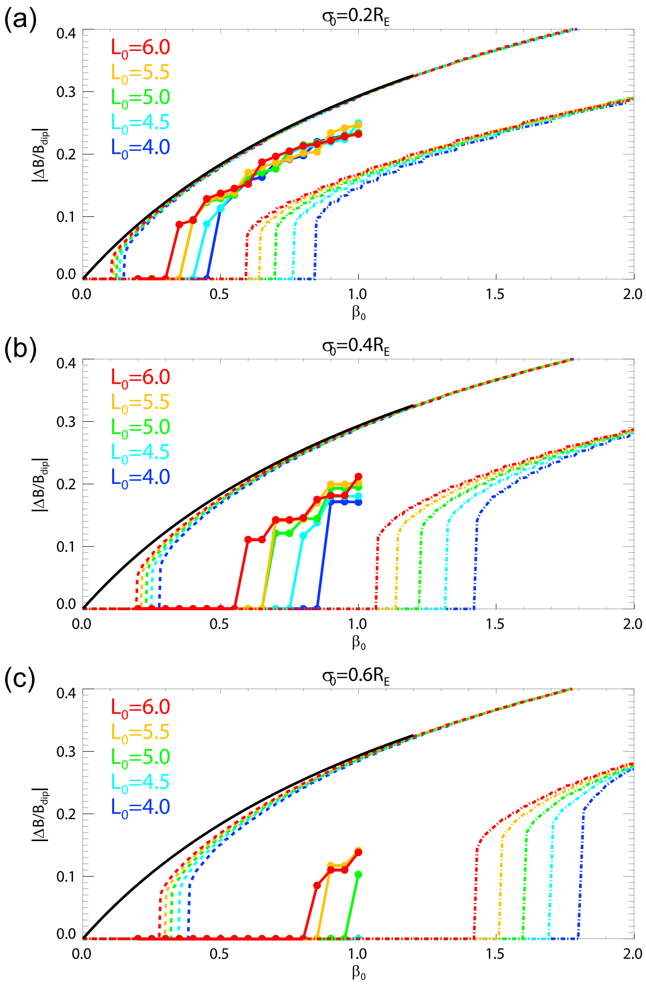

Figure 6. The relationship between the normalized dip depth ($|\Delta B/B_{\text{dipole}}|$) and β_0 for cases with different L_0 and σ_0 values. The *x* axis is β_0 and the y axis is the normalized dip depth. Panels (a)–(c) stand for $\sigma_0 = 0.2, 0.4, 0.6\ R_\text{E}$, respectively. The colored solid lines with circle symbols are model results. The black solid line is the analytical solution for uniform magnetic field. The colored dashed lines are analytical solution for circle magnetic field. The colored dash-dotted lines are analytical solution for dipole field with the assumption that the curvature keeps unchanged.

Assumptions can be made, however, to simplify the problem and to obtain approximate analytical solution to make sense of the behavior of magnetic dip. We consider the following three situations. The first and the simplest approximation to be considered is the presence of the localized plasma pressure in an initially uniform magnetic field B_0. In equilibrium, a magnetic dip forms whenever there is localized pressure distribution, and the normalized dip depth $|\Delta B/B_0|$ increases with β_0 according to $|\Delta B/B_0| = 1 - \sqrt{1/(1+\beta_0)}$ (Appendix A1), which is overplotted as the black solid line in Figure 6. The critical β_0 to form a dip is essentially zero.

The second approximation is circular and planar magnetic fields, which can be generated by an infinitely long current wire. When embedded with radially Gaussian pressure distribution $P = P_0 \exp[-(r-L_0)^2/(2\sigma_0^2)]$, the force balance equation yields an analytical solution (equation (A3) of Appendix A2). The analytical solution can be used to obtain the normalized dip depth, when the dip exists, as a function of β_0, L_0 and σ_0, which is overplotted as the colored dashed lines in Figures 6 and 7. Further analysis in Appendix A2 demonstrates that the critical β_0 for the dip formation scales as σ_0/L_0. Such analytic results reveal similar behaviors of the modeled results of equation (4), including (1) the critical β_0 increases with increasing σ_0 and decreasing L_0 (comparing the threshold β_0 values in Figure 7), (2) magnetic dip depth increases with decreasing σ_0, increasing L_0, and increasing β_0 (comparing the $|\Delta B/B_{dipole}|$ values in Figure 6), and (3) the magnetic dip tends to be independent of L_0 for larger β_0 (dashed lines with different colors merge together when β_0 is large in Figure 6).

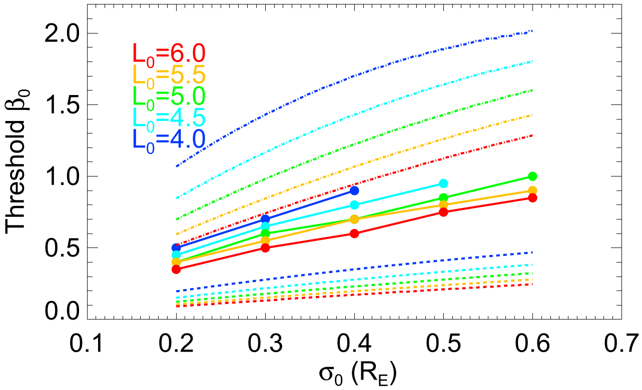

Figure 7. The critical β_0 to form the magnetic dip for cases with different L_0 and σ_0 values. The solid lines with circle symbols are results of our model. The dashed lines are results of analytic solution for circle magnetic field and the dash-dotted lines are results of analytic solution for dipole field with the assumption that the curvature keeps unchanged.

The third approximation is to ignore the change of the curvature of the dipole field, for which an analytic solution of the magnetic field radial profile can be obtained as shown in Appendix A3. The result using the analytic solution (Appendix A3) is overplotted as the colored dash-dotted lines in Figures 6 and 7. Similar behaviors of the magnetic dip are also obtained when the curvature change is ignored. The approximation, however, yields a smaller magnetic dip depth, compared with the solution of equation (4), which suggests the induced curvature change by the plasma pressure enhances the dip structure.

3.4. Comparison With 3-D SCB Model

Our 2-D axisymmetric magnetic field results are compared with 3-D RAM-SCB model (Jordanova et al., 2010) to study the effect of the azimuthal pressure distribution. We introduce a Gaussian distribution of the pressure in the azimuthal direction to represent the asymmetric ring current pressure. The pressure distribution in the equatorial plane is expressed as $P = \beta_0 P_B(L_0)\exp[-(x-L_0)^2/(2\sigma_0^2)]\exp[-(MLT-MLT_0)^2/(2\sigma_{MLT}^2)]$, where σ_{MLT} (in unit of MLT hour) denotes the width of half pressure peak in the azimuthal direction. The pressure peak is located at L_0 in the meridian plane corresponding to MLT_0 (set to 0 without loss of generality) and decays in the azimuthal direction with σ_{MLT} and in the radial direction with σ_0. Figure 8 shows the results of this 3-D model. Figures 8a and 8b show the distributions of thermal pressure and the resulting ΔB in the equatorial plane for the case with $\beta_0 = 0.65$, $L_0 = 4$, $\sigma_0 = 0.4$ R_E, $A_e = 0$, and $\sigma_{\mathrm{MLT}} = 1.0$. One can see that both the thermal pressure and ΔB magnitude maximize in the MLT_0 sector and decrease in the azimuthal direction, as expected. Figure 8c shows the variations of B versus x in the equator in the MLT_0 sector for cases with varying σ_{MLT} values, including the case of infinite σ_{MLT} denoting the azimuthally symmetric magnetic field. One can see that the magnetic field topology in the meridional plane at MLT_0 is independent of the value of σ_{MLT}, which is expected because partial derivative of the pressure with respect to MLT is zero there. However, σ_{MLT} determines the azimuthal pressure distribution and thus the azimuthal magnetic field variation. Smaller σ_{MLT} would result in larger azimuthal pressure and magnetic field gradient. The radial drift motion of energetic particles (and therefore the formation of the butterfly distribution of energetic electrons) is also affected by σ_{MLT}.

4. Conclusions and Discussion

In this study, we use axisymmetric equilibrium model to calculate SCB under a Gaussian thermal pressure distribution with four parameters: the ratio between plasma pressure and magnetic pressure at the pressure peak β_0, the radial location of the pressure peak L_0, the width of the half peak pressure σ_0 and the equatorial pressure anisotropy A_e. Then we analyze the effects of these parameters on the change of magnetic field configuration and the change of particle drifts. The main conclusions are summarized below:

- The magnetic field perturbation $|\Delta B/B_{\mathrm{dipole}}|$ increases with increasing β_0 and decreasing σ_0 and is weakly dependent of L_0 and A_e. The magnetic curvature perturbation $|\Delta R_c/R_{c,\mathrm{dip}}|$ increases with increasing A_e, increasing β_0, increasing σ_0, and decreasing L_0.
- The thermal pressure induces a change of gradient and curvature drift velocities. The induced change in the gradient drift is much greater than that in the curvature drift. The total drift change is more pronounced for larger equatorial pitch angles.
- The magnetic dip structure forms when β reaches a critical value (0.5–1). Such critical value tends to increase with increasing σ_0 and decreasing L_0 values. When the dip forms, the dip depth tends to increase with decreasing σ_0, increasing β_0 and increasing L_0 values.

In this study, we use a symmetric Gaussian distribution to approximate the radial profile of the ring current pressure distribution. The following five points are worth noting regarding the realism of the symmetric Gaussian distribution used and the realistic pressure distribution profiles that may have different width at the inner and outer edges. First, the formation of the magnetic dip (that is, the existence of a positive radial slope of the equatorial magnetic field strength) requires a strong negative radial slope of plasma β (as men-

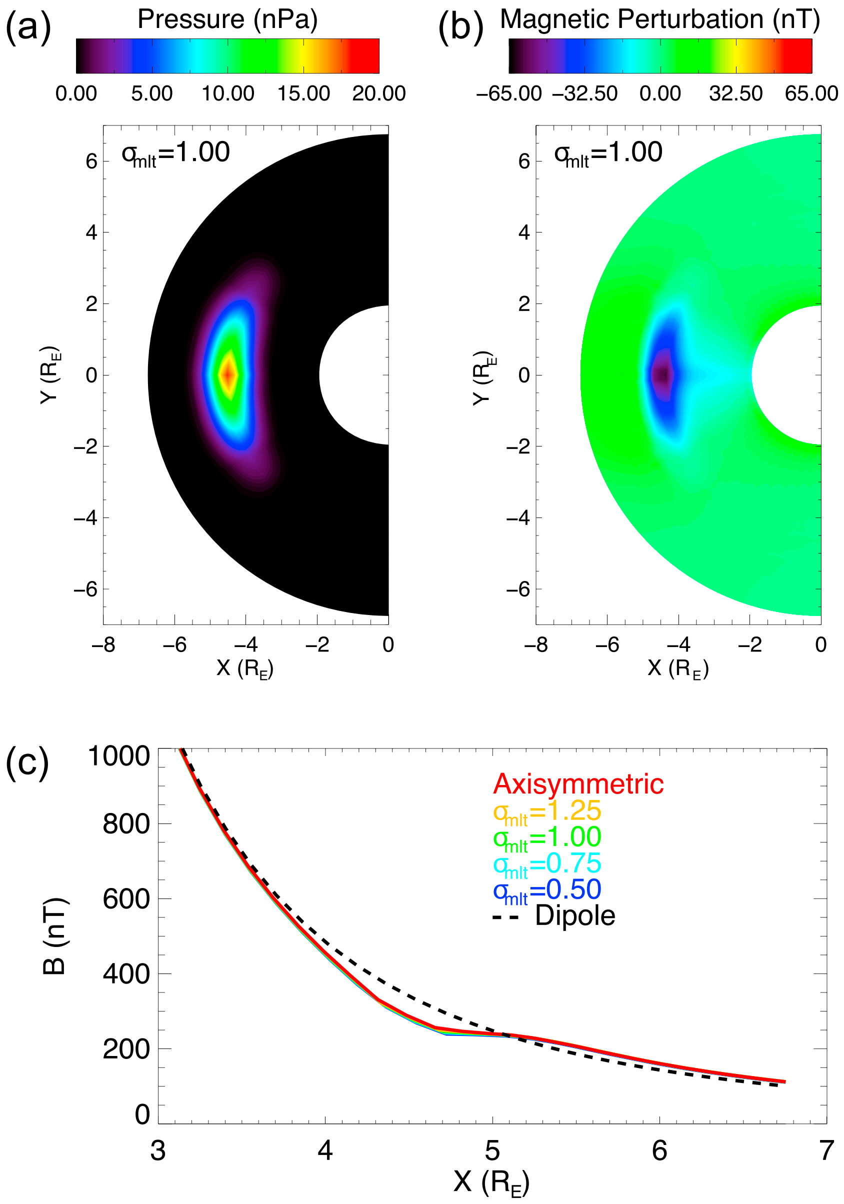

Figure 8. Three-dimensional ring current-atmosphere interactions model self-consistent magnetic field model results. (a and b) The distributions of thermal pressure and magnetic perturbation in the equatorial plane for cases with $\beta_0 = 0.65$, $L_0 = 4$, $\sigma_0 = 0.4\ R_E$, and $\sigma_{\mathrm{MLT}} = 1.0$. (c) The variations of B versus x in the equator of MLT_0 sector for cases with different σ_{MLT} values.

tioned in section 3.3), and therefore depends on the plasma β peak and the radial width of the outer edge (instead of the inner edge). One can see from Figure 2a that the magnetic dip structure (the positive slope of the magnetic field) becomes weaker as the outer width increases. The increasing inner edge width slightly decreases the magnetic field inside the pressure peak but does not affect the magnetic field strength at the pressure peak and beyond. The use of the symmetric Gaussian distribution is to help reduce the number of free parameters in the pressure distribution, and the effect of the width parameter reflects the effect of the outer edge when it comes to the formation of the magnetic dip. Second, ring current during quiet times and even moderate storms may not be able to provide a sufficiently negative radial plasma β slope and therefore the magnetic dip structures are not common in the inner magnetosphere during those times. We checked a statistical distribution of the proton pressure at midnight sector from De Michelis et al. (1999) under quiet geomagnetic condition (the top left panel in their Figure 1), which has two different radial edges with the outer edge width being slightly larger. Nonetheless the distribution near the pressure peak can be fairly well fitted by a Gaussian distribution of a radial width of ~1.1 R_E. The use of such profile in our SCB model yields no magnetic dip, even when the pressure peak increases to a value so that $\beta = 1$. This is because the statistical pressure distribution smooths out any sharp edges in the plasma pressure and has a width too large to form a dip in the magnetic field. No dip is available in the inner magnetosphere for empirical magnetic field models (except storm time magnetic field from the TS05 model as seen in Figure 1a of Ukhorskiy et al. (2006)). Third, we also check a radial distribution of plasma pressure for a specific event observed by the Arase satellite, which is shown by the black line in Figure 9e of Imajo et al. (2018). In this individual case, the Gaussian fitting approximates the observed radial pressure distribution very well of a width of about 0.5 R_E, which is narrower than that for the statistical distribution above. The plasma β for this event is also not sufficient to produce a dip, which is consistent with no dip observation for this event. Fourth, the strong connection between high plasma β and the appearance of magnetic dip has been established based on Van Allen Probes observation as shown by Figure 2 of Xiong et al. (2017) and Figure 2 of He et al. (2017). After examination of these two events, the Van Allen Probes were moving mostly in the azimuthal direction unfortunately. Therefore, the estimation of radial width of the outer edge is not available for simulating the equilibrium magnetic field profile. Finally, the plasma pressure distribution observations in the existing literatures, unfortunately, may not be ideal for checking the theoretical relation between magnetic dip and plasma pressure. One of the reasons for such unfortunateness is that this theoretical relation was not revealed before. The establishment of radial profiles of plasma pressure in the inner magnetosphere, especially for individual events, may be resolved using the observation of THEMIS satellites, which can transverse the center of ring current radially. Our theoretical relations between the radial profiles of the plasma pressure and the equilibrium magnetic field can then be checked. We leave this effort as our future investigation.

Appendix A: Analytical Solutions for the Three Approximations

A1. Uniform Magnetic Fields

Consider the presence of localized plasma pressure in an initially uniform magnetic field B_0. The analytic solution of magnetic pressure equilibrium for a uniform background magnetic field can be derived directly through the condition of uniform total pressure (that is, the sum of the magnetic pressure and the thermal pressure), $P_{B0} = P + P_B$, where P_{B0} is the magnetic pressure at the finite boundary (or the initial magnetic field pressure), P and P_B are the thermal pressure and magnetic pressure in equilibrium respectively. Thus, $|\Delta B/B_0|$ can be written as $(B_0 - B)/B_0 = 1 - B/B_0 = 1 - \sqrt{P_B/P_{B0}} = 1 - \sqrt{P_B/(P + P_B)} = 1 - \sqrt{1/(\beta + 1)}$, where $\beta = P/P_B$. In equilibrium, a magnetic dip forms whenever there is localized pressure distribution. The critical β to form a dip is essentially zero.

A2. Circular and Planar Magnetic Fields

An infinitely long straight line current can generate a circular and planar magnetic field surrounding the line current. The magnetic field strength B_0 decreases with r as

$$B_0 = \frac{\mu_0 I}{2\pi r}, \tag{A1}$$

where I is the current, r is the distance to the current, and μ_0 is the vacuum permeability.

Consider localized plasma pressure in such an initially circular and planar magnetic field. The localized pressure is introduced as $P = P_0 \exp[-(r - L_0)^2/(2\sigma_0^2)]$, with pressure peak P_0 at L_0 and half pressure peak width σ_0. In equilibrium, the force balance equation can be expressed as a 1-D nonlinear ordinary differential equation for $B(r)$:

$$\frac{1}{r}(\frac{d}{dr}(rB))B = -\mu_0 \frac{dP}{dr}. \tag{A2}$$

The corresponding analytic solution is obtained as follows:

$$B^2(r) = -2\mu_0 P_0 \exp[\frac{-(r - L_0)^2}{(2\sigma_0^2)}] - \frac{4\sigma_0^2 \mu_0 P_0 \exp[\frac{-(r-L_0)^2}{(2\sigma_0^2)}]}{r^2} + \frac{2L_0\sigma_0\mu_0 P_0 \sqrt{2\pi}\mathrm{Erf}(\frac{r-L_0}{\sqrt{2}\sigma_0})}{r^2} + \frac{C_1}{r^2}, \tag{A3}$$

where C_1 is a constant which controls the intensity of the background magnetic field. The term C_1/r^2 is the square of background magnetic field and the other terms are the perturbations caused by the thermal pressure. The pressure peak P_0 can be set as $\beta_0 P_{B0}(L_0)$, where $P_{B0}(L_0)$ is the background magnetic pressure at L_0 and equals to $C_1/2\mu_0 L_0^2$.

There are four terms on the right-hand side, and the second and the third terms can be neglected approximately due to small value of σ_0/r and $r > 1$. The remaining two terms are the first term that is contributed from thermal pressure and the last term that corresponds to the background circular magnetic field.

The condition for the existence of a magnetic dip is that there exists a local minimum, that is, $\frac{dB}{dr} = 0$. Considering only the first and last terms in equation (A3), the condition yields

$$\beta^* = \frac{2\sigma_0^2}{r_d(r_d - L_0)} = \frac{2\sigma_0^2}{(L_0 + \Delta L)\Delta L}, \tag{A4}$$

where the r_d denotes the location of the magnetic dip, $\Delta L = r_d - L_0$ is the distance between the magnetic dip and the pressure peak, and $\beta^* = 2\mu_0 P_0 \exp[\frac{-(r_d-L_0)^2}{(2\sigma_0^2)}]/(C_1/r_d^2)$ is the ratio between thermal pressure and the initial magnetic pressure at the dip. The value of ΔL scales as σ_0. Considering $L_0 + \Delta L \approx L_0$ because $L_0 \gg \Delta L$, a simplified relation can be obtained as $\beta^* \sim \sigma_0/L_0$. In other words, the critical β for the dip formation in the background circular magnetic field tends to increase for larger σ_0 and smaller L_0.

A3. Ignoring the Change of Magnetic Field Curvature

Consider the presence of isotropic thermal pressure in the background dipole field, the field line strength and curvature change in equilibrium. The force balance equation can be rewritten as

$$-\nabla_\perp P_B + 2P_B \hat{b} \cdot \nabla \hat{b} = \nabla P, \tag{A5}$$

where $P_B = \frac{B^2}{2\mu_0}$ is the magnetic pressure and $\hat{b}$ is the unit magnetic field vector. Near the equatorial plane, the curvature term $\hat{b} \cdot \nabla \hat{b}$ can be express as $-\frac{\hat{e}_r}{R_c}$ and the perpendicular gradient $\nabla_\perp$ equals to $\frac{\partial}{\partial r}\hat{e}_r$, where R_c is radius of the curvature and $\hat{e}_r$ is the unit vector in the radial direction. For dipole field, $R_c = r/3$. When we assume that the curvature of the magnetic field line remains unchanged, the equilibrium equation at the equator becomes

$$-\frac{\partial}{\partial r} P_B - \frac{6P_B}{r} = \frac{\partial}{\partial r} P. \tag{A6}$$

For the case that $P = 0$, the solution of the equation is $P_B = \frac{B^2}{2\mu_0} = Cr^{-6}$, where C is a constant. Thus, we have $B = B_0 r^{-3}$, where $B_0 = \sqrt{2\mu_0 C}$, and this is the solution of the Earth's dipole field.

For the case of a radially Gaussian pressure distribution in the equator, $P = P_0 \exp[-(r - L_0)^2/(2\sigma_0^2)]$, with pressure peak P_0 at L_0 and half pressure peak width σ_0, the analytical solution to equation (A6) is

$$\begin{aligned} P_B = &\frac{C_2}{r^6} - \frac{P_0}{r^6} \exp[\frac{-(r-L_0)^2}{2\sigma_0^2}]\{48\sigma_0^6 + r^6 + 6\sigma_0^4(4r^2 + 7r\sigma_0 + 9\sigma_0^2) + 6\sigma_0^2(r^4 + r^3\sigma_0 + r^2\sigma_0^2 + r\sigma_0^3 \\ &+ \sigma_0^4) - 3\sigma_0 \exp[\frac{(r-L_0)^2}{2\sigma_0^2}]\sqrt{2\pi}L_0(15\sigma_0^4 + 10\sigma_0^2 L_0^2 + \sigma_0^4)\mathrm{Erf}(\frac{r-L_0}{\sqrt{2}\sigma_0})\}, \end{aligned} \tag{A7}$$

where C_2 is a constant that controls the intensity of the background magnetic pressure. The term C_2/r^6 is the background dipolar magnetic pressure and the other terms are the contributions of the thermal pressure to the perturbation of magnetic pressure. The pressure peak P_0 can be set as $\beta_0 P_{B0}(L_0)$, where $P_{B0}(L_0) = C_2/L_0^6$ is the background magnetic pressure at L_0. The magnetic field strength can be obtained by $B = \sqrt{2\mu_0 P_B}$.

Acknowledgments

The SCB model simulation data used in this article are accessible at repository https://doi.org/10.5281/zenodo.2652548. The research at the University of Texas at Dallas was supported by NASA Grants NNX15AF55G and NNX17AI52G and NSF Grant 1705079 through the Geospace Environment Modeling program. The work at LANL was supported through the Laboratory Directed Research and Development program by the U.S. Department of Energy under contract DE-AC52-06NA25396.

References

Chen, L., Thorne, R. M., Jordanova, V. K., Wang, C.-P., Gkioulidou, M., Lyons, L., & Horne, R. B. (2010). Global simulation of EMIC wave excitation during the 21 April 2001 storm from coupled RMCM-RAM-Hotray modeling. *Journal of Geophysical Research*, *115*, A07209. https://doi.org/10.1029/2009JA015075

Cheng, C. Z. (1992). Magnetospheric equilibrium with anisotropic pressure. *Journal of Geophysical Research*, *97*, 1497–1510. https://doi.org/10.1029/91JA02433

De Michelis, P., Daglis, I. A., & Consolini, G. (1999). An average image of proton plasma pressure and of current systems in the equatorial plane derived from AMPTE/CCE-Chem measurements. *Journal of Geophysical Research*, *104*(A12), 28,615–28,624. https://doi.org/10.1029/1999JA900310

Fukushima, N., & Kamide, Y. (1973). Partial ring current models for worldwide geomagnetic disturbances. *Reviews of Geophysics and Space Physics*, *11*, 795–853. https://doi.org/10.1029/RG011i004p00795

Godinez, H. C., Yu, Y., Lawrence, E., Henderson, M. G., Larsen, B., & Jordanova, V. K. (2016). Ring current pressure estimation with RAM-SCB using data assimilation and Van Allen Probe flux data. *Geophysical Research Letters*, *43*, 11,948–11,956. https://doi.org/10.1002/2016GL071646

He, Z., Chen, L., Zhu, H., Xia, Z., Reeves, G. D., Xiong, Y., et al. (2017). Multiple-satellite observation of magnetic dip event during the substorm on 10 October 2013. *Geophysical Research Letters*, *44*, 9167–9175. https://doi.org/10.1002/2017GL074869

Imajo, S., Nos, M., Matsuoka, A., Kasahara, S., Yokota, S., Teramoto, M., et al. (2018). Magnetosphere-ionosphere connection of storm-time region-2 field-aligned current and ring current: Arase and ampere observations. *Journal of Geophysical Research: Space Physics*, *123*, 9545–9559. https://doi.org/10.1029/2018JA025865

Jordanova, V. K., Zaharia, S., & Welling, D. T. (2010). Comparative study of ring current development using empirical, dipolar, and self-consistent magnetic field simulations. *Journal of Geophysical Research*, *115*, A00J11. https://doi.org/10.1029/2010JA015671

Remya, B., Sibeck, D. G., Halford, A. J., Murphy, K. R., Reeves, G. D., Singer, H. J., et al. (2018). Ion injection triggered EMIC waves in the Earth's magnetosphere. *Journal of Geophysical Research: Space Physics*, *123*, 4921–4938. https://doi.org/10.1029/2018JA025354

Santolík, O. (2008). New results of investigations of whistler-mode chorus emissions. *Nonlinear Processes in Geophysics*, *15*, 621–630.

Tenerani, A., Le Contel, O., Califano, F., Robert, P., Fontaine, D., Cornilleau-Wehrlin, N., & Sauvaud, J.-A. (2013). Cluster observations of whistler waves correlated with ion-scale magnetic structures during the 17 August 2003 substorm event. *Journal of Geophysical Research: Space Physics*, *118*, 6072–6089. https://doi.org/10.1002/jgra.50562

Tsurutani, B. T., Verkhoglyadova, O. P., Lakhina, G. S., & Yagitani, S. (2009). Properties of dayside outer zone chorus during HILDCAA events: Loss of energetic electrons. *Journal of Geophysical Research*, *114*, A03207. https://doi.org/10.1029/2008JA013353

Tsyganenko, N. A. (2000). Modeling the inner magnetosphere: The asymmetric ring current and Region 2 Birkeland currents revisited. *Journal of Geophysical Research*, *105*, 27,739–27,754. https://doi.org/10.1029/2000JA000138

Tsyganenko, N. A., & Sitnov, M. I. (2005). Modeling the dynamics of the inner magnetosphere during strong geomagnetic storms. *Journal of Geophysical Research*, *110*, A03208. https://doi.org/10.1029/2004JA010798

Ukhorskiy, A. Y., Anderson, B. J., Brandt, P. C., & Tsyganenko, N. A. (2006). Storm time evolution of the outer radiation belt: Transport and losses. *Journal of Geophysical Research*, *111*, A11S03. https://doi.org/10.1029/2006JA011690

Xia, Z., Chen, L., Zheng, L., & Chan, A. A. (2017). Eigenmode analysis of compressional poloidal modes in a self-consistent magnetic field. *Journal of Geophysical Research: Space Physics*, *122*, 10,369–10,381. https://doi.org/10.1002/2017JA024376

Xiao, F., & Feng, X. (2006). Modeling density and anisotropy of energetic electrons along magnetic field lines. *Plasma Science and Technology*, *8*, 279–284. https://doi.org/10.1088/1009-0630/8/3/07

Xiong, Y., Chen, L., Xie, L., Fu, S., Xia, Z., & Pu, Z. (2017). Relativistic electron's butterfly pitch angle distribution modulated by localized background magnetic field perturbation driven by hot ring current ions. *Geophysical Research Letters*, *44*, 4393–4400. https://doi.org/10.1002/2017GL072558

Yu, Y., Jordanova, V., Zaharia, S., Koller, J., Zhang, J., & Kistler, L. M. (2012). Validation study of the magnetically self-consistent inner magnetosphere model RAM-SCB. *Journal of Geophysical Research*, *117*, A03222. https://doi.org/10.1029/2011JA017321

Yue, C., Wang, C.-P., Lyons, L., Liang, J., Donovan, E. F., Zaharia, S. G., & Henderson, M. (2014). Current sheet scattering and ion isotropic boundary under 3-D empirical force-balanced magnetic field. *Journal of Geophysical Research: Space Physics*, *119*, 8202–8211. https://doi.org/10.1002/2014JA020172

Yue, C., Wang, C.-P., Nishimura, Y., Murphy, K. R., Xing, X., Lyons, L., et al. (2015). Empirical modeling of 3-D force-balanced plasma and magnetic field structures during substorm growth phase. *Journal of Geophysical Research: Space Physics*, *120*, 6496–6513. https://doi.org/10.1002/2015JA021226

Yue, C., Wang, C.-P., Zaharia, S. G., Xing, X., & Lyons, L. (2013). Empirical modeling of plasma sheet pressure and three-dimensional force-balanced magnetospheric magnetic field structure: 2. Modeling. *Journal of Geophysical Research: Space Physics*, *118*, 6166–6175. https://doi.org/10.1002/2013JA018943

Zaharia, S., Cheng, C., & Maezawa, K. (2004). 3-D force-balanced magnetospheric configurations. *Annales Geophysicae*, *22*, 251–265. https://doi.org/10.5194/angeo-22-251-2004

Zaharia, S., Jordanova, V. K., Thomsen, M. F., & Reeves, G. D. (2006). Self-consistent modeling of magnetic fields and plasmas in the inner magnetosphere: Application to a geomagnetic storm. *Journal of Geophysical Research*, *111*, A11S14. https://doi.org/10.1029/2006JA011619

Zhima, Z., Cao, J., Fu, H., Liu, W., Chen, L., Dunlop, M., et al. (2015). Whistler mode wave generation at the edges of a magnetic dip. *Journal of Geophysical Research: Space Physics*, *120*, 2469–2476. https://doi.org/10.1002/2014JA020786